

Fault Diagnosis of Sensors for T-type Three-Level Inverter-fed Dual Three-Phase Permanent Magnet Synchronous Motor Drives

Research Article

Xueqing Wang, Zheng Wang, Wei Wang, Ming Cheng

Southeast University, Nanjing, China

Received March 04, 2018; Accepted July 07, 2018

Abstract: To improve the reliability of motor system, this paper investigates the sensor fault diagnosis methods for T-type inverter-fed dual three-phase permanent magnet synchronous motor (PMSM) drives. Generally, a T-type three-level inverter-fed dual three-phase motor drive utilizes four phase-current sensors, two direct current (DC)-link voltage sensors and one speed sensor. A series of diagnostic methods have been comprehensively proposed for the three types of sensor faults. Both the sudden error change and gradual error change of sensor faults are considered. Firstly, the diagnosis of speed sensor fault was achieved by monitoring the error between the rotating speed of stator flux and the value from speed sensor. Secondly, the large high-frequency voltage ripple of voltage difference between the estimated voltage and the reference voltage was used to identify the voltage sensor faults, and the faulty voltage sensor was determined according to the deviation of voltage difference. Thirdly, the abnormal current amplitude on harmonic subspace was adopted to identify the current sensor faults, and the faulty current sensor was located by distinguishing the current trajectory on harmonic subspace. The experiments have been taken on a laboratory prototype to verify the effectiveness of the proposed fault diagnosis schemes.

Keywords: *fault diagnosis • sensor fault • T-type three-level inverter • dual three-phase PMSM*

1. Introduction

Recently, with the increasing demands of high reliability and large capacity for motor systems, multiphase drives have been widely applied in various fields such as electric elevator, aerospace, electric vehicle and ship propulsion (Levi et al. 2016; Mengoni et al. 2015; Umesh and Sivakumar 2016). The main advantages of multiphase motor drives are as follows (Bojoi et al. 2005; Jahns 1980; Wang et al. 2017b) : low torque ripple, low current stress on inverter and motor stator, high power density, large power rating, good fault-tolerant capability and more flexible control methods. On the other hand, T-type three-level inverter becomes more popular for low-voltage and high-reliability applications, because of its superior harmonic performance and better fault tolerance (Choi et al. 2014, 2015). The T-type three-level inverter-fed dual three-phase permanent magnet synchronous motor (PMSM) drive system combines the advantages of T-type three-level inverters and multiphase motor drives (Wang et al. 2017a, 2018b).

There are mainly three kinds of faults in a motor system: mechanical, electrical and sensor faults. Stator faults and inverter faults are usually defined as electrical faults, including short-circuit fault and open-circuit fault (Romary et al. 2010; Sleszynski et al., 2009). A comprehensive review of the diagnostic methods for the mechanical and electrical faults is presented in Bellini et al. (2008). On the other hand, sensor faults are also one of the most common problems in the practical application of electric drive.

* Email: wangxueqing231@163.com, zwwang@eee.hku.hk, wangwei1986@seu.edu.cn, mcheng@seu.edu.cn

Generally, a T-type three-level inverter-fed dual three-phase motor drive utilizes four phase-current sensors, two direct current (DC)-link voltage sensors and one speed sensor. In recent years, many works have been performed on sensor fault diagnosis in motor system. In Najafabadi et al. (2011), an adaptive observer is adopted to identify three kinds of sensor faults by estimating phase currents, rotor fluxes and rotor resistance. The outputs of the adaptive observer are provided for a decision-making unit to find the type and location of the faulty sensor. A fault diagnosis scheme for PMSM drives based on an extended Kalman filter is presented in Foo et al. (2013). The fault of any sensor in three-phase PMSM drives can be identified and isolated to ensure uninterrupted operation. In Salmasi (2017), phase-current asymmetry is adopted as a detection method for current sensor fault, and speed sensor fault is identified when the field component and torque component of stator currents are not perpendicular to each other. In Berriri et al. (2012), a parity space method is adopted to diagnose the faults of current sensors and voltage sensors. The fault identification method is robust to parameter variations, but only applicable for sudden change of sensor signal.

Although the aforementioned studies of fault diagnosis have made great efforts for improving the reliability of motor drives, no research about sensor fault diagnosis of multiphase motor drives has been conducted. In addition, the diagnostic method for voltage sensor faults in three-level inverter is still unknown. Different from previous studies, the contributions of this paper are as follows: 1) the impacts of all sensor faults and the related diagnostic methods of T-type three-level inverter-fed dual three-phase PMSM drive were investigated comprehensively; 2) both the sudden error change and gradual error change of sensor faults were detected; 3) the large high-frequency voltage ripple of voltage difference between the estimated voltage and the reference voltage was used to identify the voltage sensor faults, and the faulty voltage sensor was determined according to the deviation of voltage difference; 4) the abnormal current amplitude on x - y subspace was adopted to identify the current sensor faults, and the faulty current sensor was located by distinguishing the current trajectory on x - y subspace under faulty state; 5) no additional hardware was required to achieve all the proposed fault diagnosis methods.

The rest of this paper is organized as follows: The machine model and basic control of T-type three-level inverter-fed dual three-phase PMSM motor drive are described in Section 2. In Sections 3, 4 and 5, speed sensor fault, voltage sensor fault and current sensor fault are analyzed, respectively, and the corresponding fault diagnosis methods are designed. In Section 6, the effectiveness of the proposed diagnostic methods for different types of sensor faults is verified by experimental test. Finally, conclusions are drawn in Section 7.

2. Machine model and basic control

Fig. 1 shows the configuration of the T-type three-level inverter-fed dual three-phase PMSM drives. This system combines the advantages of T-type three-level topology and multiphase motor drives. The dual three-phase PMSM drive in this paper has two sets of three-phase windings, which are spatially shifted 30 electrical degrees with isolated neutrals.

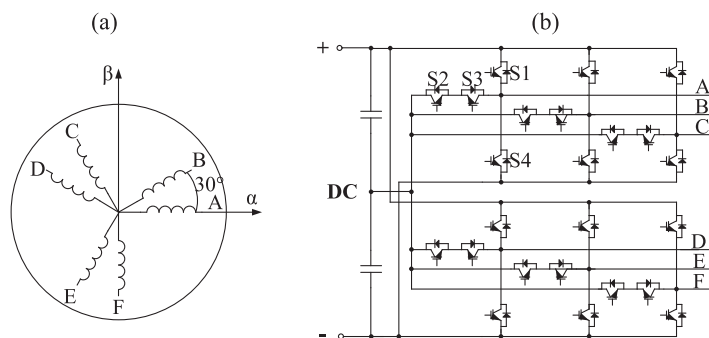


Fig. 1. Dual three-phase PMSM drive: (a) dual three-phase PMSM; (b) six-phase T-type three-level inverter

2.1. Modelling of dual three-phase PMSM

The dual three-phase PMSM is a non-linear high-order system, which makes the analysis and control difficult. By using vector space decomposition (VSD), the voltage and current space vectors of the dual three-phase PMSM can be decoupled into three two-dimensional orthogonal subspaces: α - β subspace (torque subspace), x - y subspace (harmonic subspace) and o_1 - o_2 subspace (Zhao and Lipo, 1995). Eq. (1) shows the decomposition matrix for VSD:

$$\begin{bmatrix} \alpha \\ \beta \\ x \\ y \\ o_1 \\ o_2 \end{bmatrix} = \frac{1}{3} \begin{bmatrix} 1 & -\frac{1}{2} & -\frac{1}{2} & \frac{\sqrt{3}}{2} & -\frac{\sqrt{3}}{2} & 0 \\ 0 & \frac{\sqrt{3}}{2} & -\frac{\sqrt{3}}{2} & \frac{1}{2} & \frac{1}{2} & -1 \\ 1 & -\frac{1}{2} & -\frac{1}{2} & -\frac{\sqrt{3}}{2} & \frac{\sqrt{3}}{2} & 0 \\ 0 & -\frac{\sqrt{3}}{2} & \frac{\sqrt{3}}{2} & \frac{1}{2} & \frac{1}{2} & -1 \\ 1 & 1 & 1 & 0 & 0 & 0 \\ 0 & 0 & 0 & 1 & 1 & 1 \end{bmatrix} \begin{bmatrix} A \\ B \\ C \\ D \\ E \\ F \end{bmatrix} \quad (1)$$

According to Eq. (1), a four-dimensional equation can be obtained. The corresponding voltage, flux and torque equations are listed as follows:

$$\begin{bmatrix} u_d \\ u_q \\ u_x \\ u_y \end{bmatrix} = \begin{bmatrix} R_s & 0 & 0 & 0 \\ 0 & R_s & 0 & 0 \\ 0 & 0 & R_s & 0 \\ 0 & 0 & 0 & R_s \end{bmatrix} \begin{bmatrix} i_d \\ i_q \\ i_x \\ i_y \end{bmatrix} + \frac{d}{dt} \begin{bmatrix} \psi_d \\ \psi_q \\ \psi_x \\ \psi_y \end{bmatrix} + \omega \begin{bmatrix} -\psi_q \\ \psi_d \\ 0 \\ 0 \end{bmatrix} \quad (2)$$

$$\begin{bmatrix} \psi_d \\ \psi_q \\ \psi_x \\ \psi_y \end{bmatrix} = \begin{bmatrix} L_d & 0 & 0 & 0 \\ 0 & L_q & 0 & 0 \\ 0 & 0 & L_{xy} & 0 \\ 0 & 0 & 0 & L_{xy} \end{bmatrix} \begin{bmatrix} i_d \\ i_q \\ i_x \\ i_y \end{bmatrix} + \begin{bmatrix} 1 \\ 0 \\ 0 \\ 0 \end{bmatrix} \psi_f \quad (3)$$

$$T_e = 3n_p (\psi_d i_q - \psi_q i_d) \quad (4)$$

where $L_d = L_{ls} + 3L_{ms} + 3L_{mr}$, $L_q = L_{ls} + 3L_{ms} - 3L_{mr}$ and $L_{xy} = L_{ls}$. L_{ms} is the stator mutual inductance, L_{ls} is the stator leakage inductance and n_p is the pole pair number.

2.2. Space Vector Modulation based Direct Torque Control (SVM-DTC) for dual three-phase PMSM

Fig. 2 shows the control diagram of SVM-DTC scheme for T-type three-level inverter-fed dual three-phase PMSM (Wang et al., 2018a). The amplitude U_{ref} and angle θ_{ref} of reference voltage vector are predicted based on the error of torque angle $\Delta\delta$ and the actual stator flux ψ_s . To eliminate the undesirable current harmonics, the reference voltage vector is synthesized through a VSD-based two-step voltage vector synthesis SVM: The first step is to use inverter voltage vectors to compose harmonic-free vectors by forcing the average volt seconds of voltage vectors on x - y subspace to be zero. The second step is to utilize two adjacent harmonic-free vectors to synthesize the reference voltage vector based on volt-second balance principle.

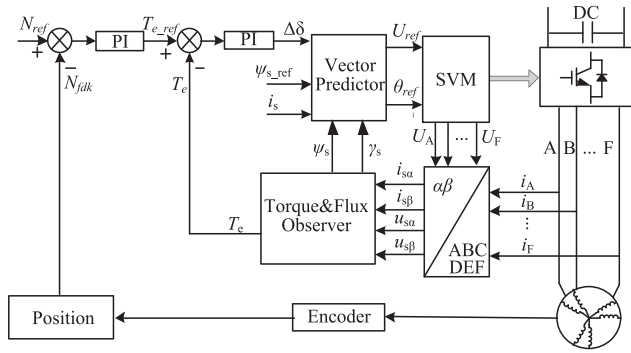


Fig. 2. Control diagram of classical SVM-DTC for dual three-phase PMSM

3. Diagnosis of speed sensor fault

Speed sensor is usually used to acquire the position and speed of rotor. In practical application, vector control has to acquire both position and speed of rotor. By comparison, direct torque control requires only speed information. Therefore, the adopted SVM-DTC scheme has better speed sensor fault-tolerant capability. The worst situation of speed sensor fault is that the whole speed signal disappears. In this case, the measured speed will drop to zero swiftly. Then, the actual speed will increase to a maximum value limited by DC-link voltage. The uncontrollable high speed will cause serious overload and dangerous damage to the motor system.

The rotor angular speed can be estimated as follows (Parsa and Toliyat, 2007):

$$N_{et} = \frac{d}{dt} \theta = \frac{d}{dt} (\lambda_s + \delta) = N_\psi + N_d \approx N_\psi \quad (5)$$

where, θ is the rotor angle, λ_s is the angle of stator flux and δ is the torque angle. N_ψ is the speed of stator flux relative to stator, and N_d is its speed relative to rotor. In steady state, δ is a constant value and then N_d is equal to zero. In dynamic state, because the change rate of the torque is small, N_d can also be neglected. Therefore, it is a simple and effective method to estimate the rotor angle speed with the rotating speed of stator flux. When speed sensor fault occurs, the error between the feedback speed N_{fdbk} and the estimated speed N_{et} would go beyond the predetermined threshold and the speed sensor fault is identified. In this paper, the ratio of absolute error to rated speed, namely speed index, is compared with the predetermined threshold to monitor speed sensor fault.

4. Diagnosis of voltage sensor fault

The measured DC-link voltage and mid-point voltage participate in flux estimation, vector prediction and space vector synthesis in the adopted SVM-DTC scheme for dual three-phase PMSM. According to the faulty severity, the voltage sensor fault can be classified into two cases. The first case is that the error of measured voltage increases suddenly by a large margin, which will directly cause the breakdown of motor system. In this case, the voltage sensor fault is required to be rapidly detected in several sampling periods. The second case is that the error of measured voltage changes gradually or suddenly by a small margin and the motor system can still work in faulty state.

In normal operation, the change of DC-link voltage in one sampling period is limited in a small range. The limit value can be acquired by practical measurement. Therefore, the threshold of diagnosis for the first case can be obtained by adding enough margin to the limit value. When the absolute difference between voltage in previous sampling period and present voltage exceeds predetermined threshold, the voltage sensor fault can be detected immediately (Foo et al., 2015). Because this diagnostic method is designed based on large voltage change, it is not applicable to the case when the error of measured voltage changes gradually or suddenly by a small margin.

When the second case of voltage sensor fault occurs, large high-frequency voltage ripple will be found in the feedback voltage u_{fdk} , which can be obtained from Eq. (6). The reason is that the positive small vectors and negative small vectors have the same effect on magnetic field in the normal state. In the fault state of voltage sensor, the positive small vectors and negative small vectors have different effects on magnetic field, because of the unbalanced capacitor voltages. Therefore, large high-frequency voltage ripple occurs in the switching process between the positive small vectors and negative small vectors. To differentiate the faults of DC-link voltage sensor and mid-point voltage sensor, the voltage difference ΔU between the feedback voltage u_{fdk} and the reference voltage U_{ref} is introduced. The fault in mid-point voltage sensor will not cause the deviation of voltage difference ΔU , but the fault in DC-link voltage sensor will cause the deviation. Therefore, the large high-frequency voltage ripple of voltage difference ΔU can be used to identify the voltage sensor faults, and the specific voltage sensor fault can be determined according to the deviation of voltage difference ΔU .

$$\begin{cases} u_{fdk} = \sqrt{u_d^2 + u_q^2} \\ u_d = R_s i_d + L_d \frac{di_d}{dt} - \omega L_q i_q \\ u_q = R_s i_q + L_q \frac{di_q}{dt} + \omega L_d i_d + \omega \psi_f \end{cases} \quad (6)$$

5. Diagnosis of current sensor fault

Four current sensors are utilized to measure the currents of phase A, phase B, phase D and phase E in the adopted motor system. Similar to voltage sensor fault, current sensor faults could be no signal output, incorrect gain and DC bias. Due to the large phase number in dual three-phase PMSM, even the most serious case of current sensor fault, namely zero output, will not cause breakdown of motor system. Therefore, the diagnosis of current sensor fault has no rigorous time limit. According to Eq. (1), the currents of x -axis and y -axis can be simplified as:

$$\begin{cases} i_x = \frac{1}{6} (3i_A - \sqrt{3}i_D - \sqrt{3}i_E) \\ i_y = \frac{1}{6} (-\sqrt{3}i_A - 2\sqrt{3}i_B + 3i_D + 3i_E) \end{cases} \quad (7)$$

The calculated amplitude of current on x - y subspace is incorrect and large, due to the incorrect feedback value of faulty current sensor. For example, when the current sensor of phase A fails, the feedback value of phase A current i_{A_fdk} can be regarded as the superposition of the real value i_{A_rl} and the error i_{A_err} .

$$i_{A_fdk} = i_{A_rl} + i_{A_err} \quad (8)$$

Because the real current on x - y subspace is close to zero under current sensor fault, both the real currents of x -axis and y -axis, namely i_{x_rl} and i_{y_rl} , are almost zero. Therefore, the feedback values of x -axis current and y -axis current, namely i_{x_fdk} and i_{y_fdk} , can be estimated as follows:

$$\begin{cases} i_{x_fdk} = \frac{1}{2} i_{A_err} + i_{x_rl} \approx \frac{1}{2} i_{A_err} \\ i_{y_fdk} = -\frac{\sqrt{3}}{2} i_{A_err} + i_{y_rl} \approx -\frac{\sqrt{3}}{2} i_{A_err} \end{cases} \quad (9)$$

According to Eq. (9), it is inferred that the current trajectory on x - y subspace moves along a straight line with fixed slope. Different current trajectories under different current sensor faults can be plotted on x - y subspace, as shown in Fig. 3.

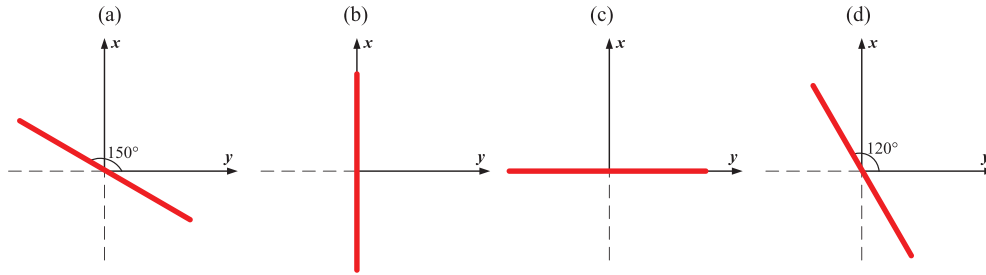


Fig. 3. Current trajectories of different current sensor faults on x - y subspace: (a) fault in phase A; (b) fault in phase B; (c) fault in phase D; (d) fault in phase E

A current comparison method is proposed to identify the direction of current trajectory. At first, the current components of six axes are obtained by phase current as follows:

$$\begin{bmatrix} i_{x1} \\ i_{y1} \\ i_{x2} \\ i_{y2} \\ i_{x3} \\ i_{y3} \end{bmatrix} = \frac{1}{6} \begin{bmatrix} 2 & -1 & -1 & \sqrt{3} & -\sqrt{3} & 0 \\ 0 & -\sqrt{3} & \sqrt{3} & 1 & 1 & -2 \\ -1 & -1 & 2 & \sqrt{3} & 0 & -\sqrt{3} \\ -\sqrt{3} & \sqrt{3} & 0 & 1 & -2 & 1 \\ -1 & 2 & -1 & 0 & -\sqrt{3} & \sqrt{3} \\ \sqrt{3} & 0 & -\sqrt{3} & -2 & 1 & 1 \end{bmatrix} \begin{bmatrix} i_A \\ i_B \\ i_C \\ i_D \\ i_E \\ i_F \end{bmatrix} \quad (9)$$

The average absolute value of current component along each axis within one fundamental period is used for judgement. The faulty current sensor is thus identified by seeking out the axis with smallest current component, since the current component is smallest in the axis perpendicular to the current trajectory.

6. Experimental verification

The experiments were carried out on a laboratory prototype of T-type three-level inverter-fed dual three-phase PMSM drive to verify the effectiveness of the proposed fault diagnostic scheme. In the experiment, all sensors functioned as expected and different sensor faults were simulated by replacing the normal sampling signal with the faulty one. The operation states of all sensors were controllable, and only one sensor fault was set at one moment in the experiment. Fig. 4 shows the image of the experimental setup. In the experiments, the digital signal processor (DSP) performed the control algorithm and generated the 12-channel pulse-width modulation (PWM) signals, which were transported into 24-channel complementary PWM signals by digital dead-time generator. The power inverters were built with six T-type modules to supply the dual three-phase PMSM machine. A permanent magnet (PM) generator was coupled to the PMSM machine to work as an electric load. The key parameters of the experimental setup are summarized in Table 1.

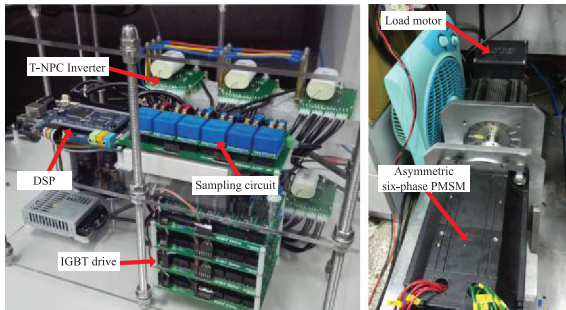


Fig. 4. Experimental setup

Table 1. Parameters of experimental setup

Name	Value
Pole pair number	3
q-axis inductance	6.21 mH
d-axis inductance	6.21 mH
PM flux (amplitude)	0.2 Wb
Resistor	0.21 Ω
DC-link capacitor	1000 μ F
DC-link voltage	200 V
Speed sampling period	10 ms
Rated speed	1000 rpm
Rated load torque	10 Nm

In order to show the diagnosis results on the scope clearly, three fault signals, namely FL0, FL1, and FL2, are adopted to express the specific fault. Signal FL0 will become 1, when abnormal operation is detected. Signal FL1 and signal FL2 will act when a specific fault is located. Signal FL1 represents the location of the fault. Signal FL2 represents the specific fault types. If both signal FL1 and signal FL2 remain 0, the drive system operates in normal state. The values of signal FL2, 1, 2, 3 and 5, indicate the occurrence of speed sensor fault, voltage sensor fault in DC link, mid-point voltage sensor fault and current sensor fault. If current sensor fault occurs, the values of signal FL1, 1, 2, 4 and 5, indicate the faulty current sensors of phase A, phase B, phase D and phase E, respectively.

Fig. 5 shows the dynamic performance of SVM-DTC for dual three-phase PMSM drive under normal state. The speed reference is shifted between 200 rpm and 1000 rpm. The edge counter is introduced to count the number of voltage ripple edges in voltage difference ΔU . It is obvious that the speed index, current amplitude on x - y subspace I_{xy} and voltage edge number are all below their respective threshold values, which indicates that no fault occurs during both dynamic and steady states.

Fig. 6 shows the performance of fault diagnosis and tolerance for speed sensor fault. The speed reference N_{ref} is 1000 rpm. A most serious case of speed sensor fault is considered in the experiments. All the pulse signals from encoder disappear. After the speed sensor fault occurs, the feedback value of speed drops to zero in one speed-sampling period, as shown in Fig. 6(a). Then, the output of speed proportional integral (PI) controller is saturated and the actual speed N_{rl} increases to a maximum value limited by DC-link voltage. It is observed that the estimated speed N_{et} can track the real speed N_{rl} precisely. The speed index exceeds its threshold 0.1, as soon as the feedback value of speed drops to zero as shown in Fig. 6(b), and the speed sensor fault can be identified directly, as shown in Fig. 6(c).

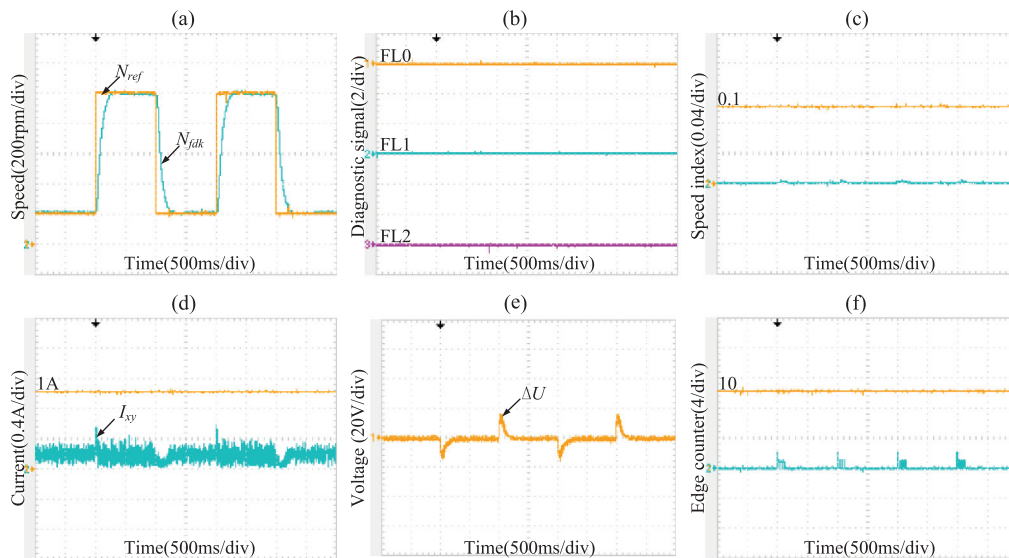


Fig. 5. Dynamic performance without fault: (a) speed; (b) fault location signal; (c) speed diagnosis; (d) amplitude of current on harmonic subspace; (e) the difference between voltage reference and estimated voltage; (f) voltage edge counter

Fig. 7 shows the diagnostic process of serious voltage sensor fault in DC link. At the time of fault occurrence (FO), the feedback voltage U_{dc_fdk} changes to zero immediately, as shown in Fig. 7(a). The absolute difference between voltage in previous sampling period and present voltage which exceeds predetermined threshold and the voltage sensor fault in DC link are detected immediately, as shown in Fig. 7(b). The voltage sensor fault in DC link will not cause the misdiagnosis of other faults, as shown in Fig. 7(c). Thus, similar serious voltage sensor fault in DC link will cause the sudden breakdown of motor system. To avoid the serious influence, the incorrect feedback voltage is replaced with a constant voltage value which is close to the real DC-link voltage. Similar fault diagnostic methods are applied in the serious mid-point voltage sensor fault, as shown in Fig. 8.

Fig. 9 shows the performance of diagnostic method for the second case of DC-link voltage sensor fault. The error percentage of feedback voltage is set to uniformly increase from 0 to 20% in 200 ms. It can be seen that the feedback DC-link voltage U_{dc_fdk} deviates the real DC-link voltage U_{dc_rl} gradually after fault as shown in Fig. 9(a). The ripple of voltage difference ΔU increases gradually, and the edge counter exceeds predetermined threshold 10, as shown in Fig. 9(b) and (c). The average voltage difference also goes beyond its own threshold 3 V as shown in Fig. 9(d). According to the two diagnostic conditions as shown in Fig. 9(c) and (d), the DC-link voltage sensor fault is identified, as shown in Fig. 9(e). The voltage sensor fault in DC link will not cause the misdiagnosis of other faults, as shown in Fig. 9(f) and (g).

Fig. 10 shows the performance of diagnostic method for the second case of mid-point voltage sensor fault. The error percentage of feedback voltage is set to uniformly increase from 0 to 20% in 200 ms. It can be seen that the feedback mid-point voltage U_{dc_fdk} deviates the real mid-point voltage U_{dc_rl} gradually after fault as shown in Fig. 10(a). The ripple of voltage difference ΔU increases gradually, and the edge counter exceeds predetermined

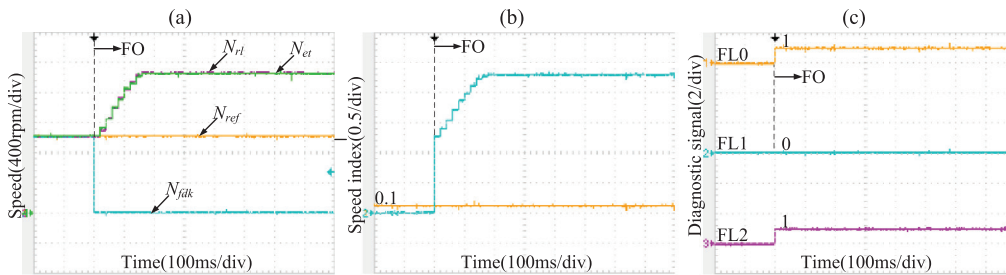


Fig. 6. Diagnostic process of speed sensor fault: (a) speed; (b) speed diagnosis; (c) fault location signal

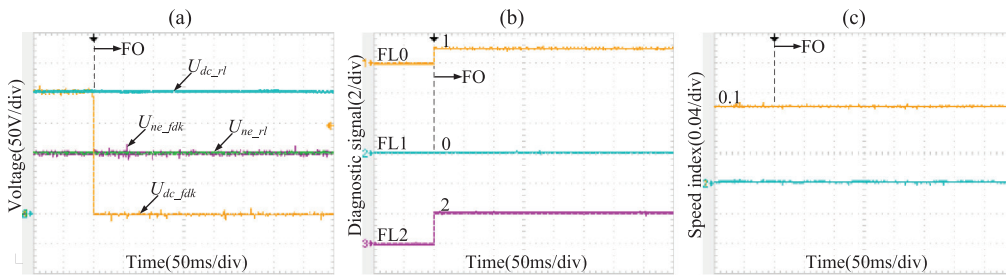


Fig. 7. Diagnostic process of serious voltage sensor fault in DC-link: (a) DC-link voltage and mid-point voltage of DC link; (b) fault location signal; (c) speed diagnosis

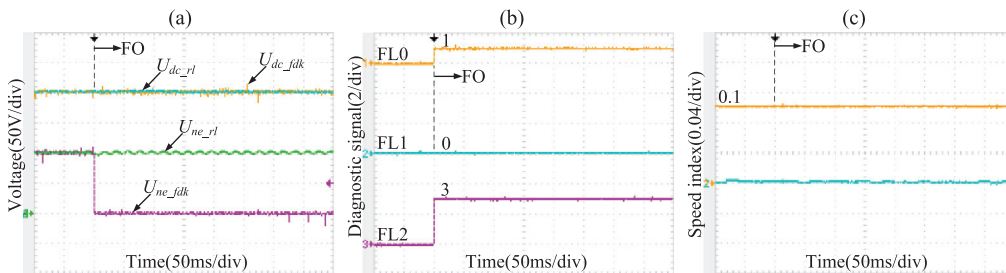


Fig. 8. Diagnostic process of serious voltage sensor fault in mid-point of DC link: (a) DC-link voltage and mid-point voltage of DC link; (b) fault location signal; (c) speed diagnosis

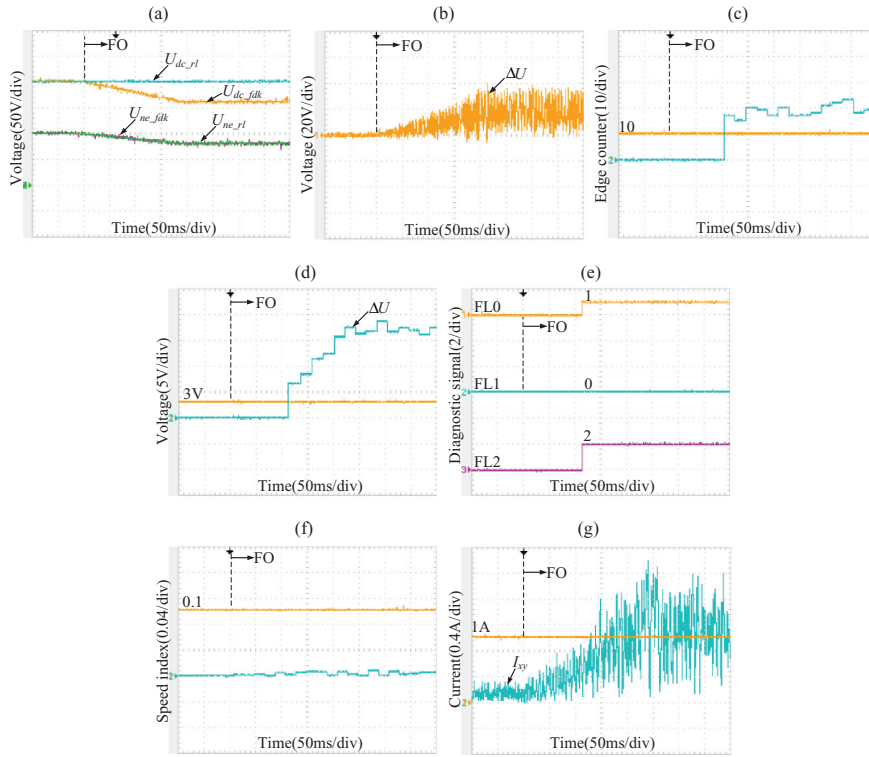


Fig. 9. Diagnostic process of general voltage sensor fault in DC link: (a) DC-link voltage and mid-point voltage of DC link; (b) the difference between voltage reference and estimated voltage; (c) voltage edge counter; (d) average voltage diagnosis; (e) fault location signal; (f) speed diagnosis; (g) amplitude of current on harmonic subspace

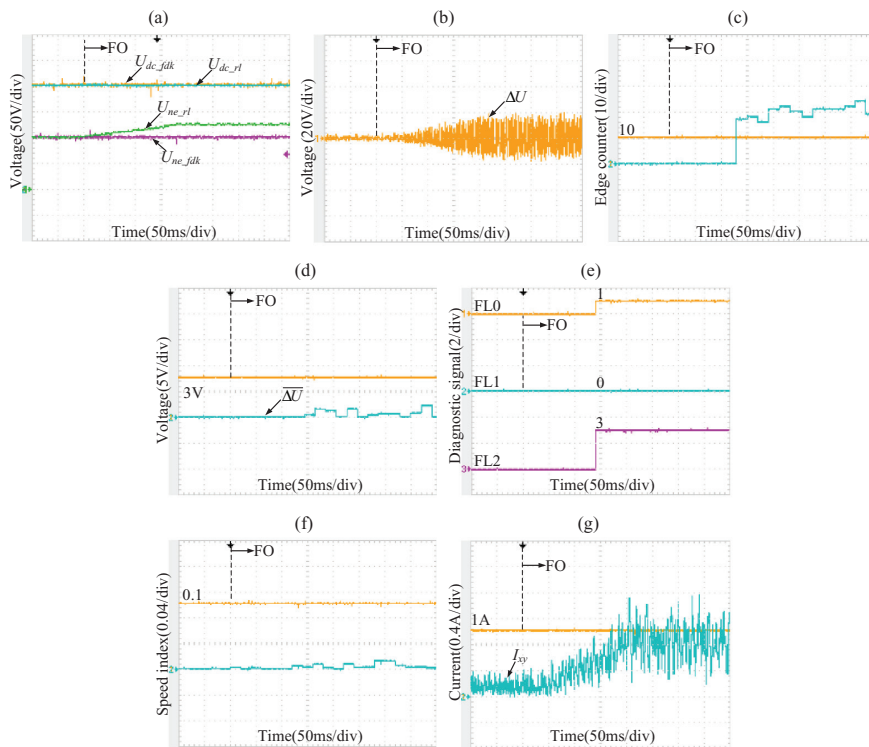


Fig. 10. Diagnostic process of general voltage sensor fault in mid-point of DC link: (a) DC-link voltage and mid-point voltage of DC link; (b) the difference between voltage reference and estimated voltage; (c) voltage edge counter; (d) average voltage diagnosis; (e) fault location signal; (f) speed diagnosis; (g) amplitude of current on harmonic subspace

threshold 10, as shown in Fig. 10(b) and (c). The average voltage difference remains low as shown in Fig. 10(d). According to the two diagnostic conditions as shown in Fig. 10(c) and (d), the mid-point voltage sensor fault is identified, as shown in Fig. 10(e). The mid-point voltage sensor fault will not cause the misdiagnosis of other faults, as shown in Fig. 10(f) and (g).

Fig. 11 shows the performance of diagnosis and fault tolerance for current sensor fault in phase A. The feedback value of current sensor in phase A is forced to be zero at FO. After fault occurs, the phase currents become asymmetric, as shown in Fig. 11(a) and (b). The amplitude of current on x - y subspace I_{xy} exceeds its threshold 1A, and the abnormal current is detected immediately as shown in Fig. 11(c) and (d). Then, it takes one fundamental period to identify the specific fault. The current trajectory on x - y subspace as shown in Fig. 11(e) is same with the expected result as shown in Fig. 3. Since the minimum one of six average absolute currents is i_{x3} , as shown in Fig. 11(f)–(h). Therefore, the current trajectory on x - y subspace moves along i_{y3} axis, and the current sensor fault in phase A is finally identified, as shown in Fig. 11(i). The current sensor fault will not cause the misdiagnosis of other faults, as shown in Fig. 11(j)–(l).

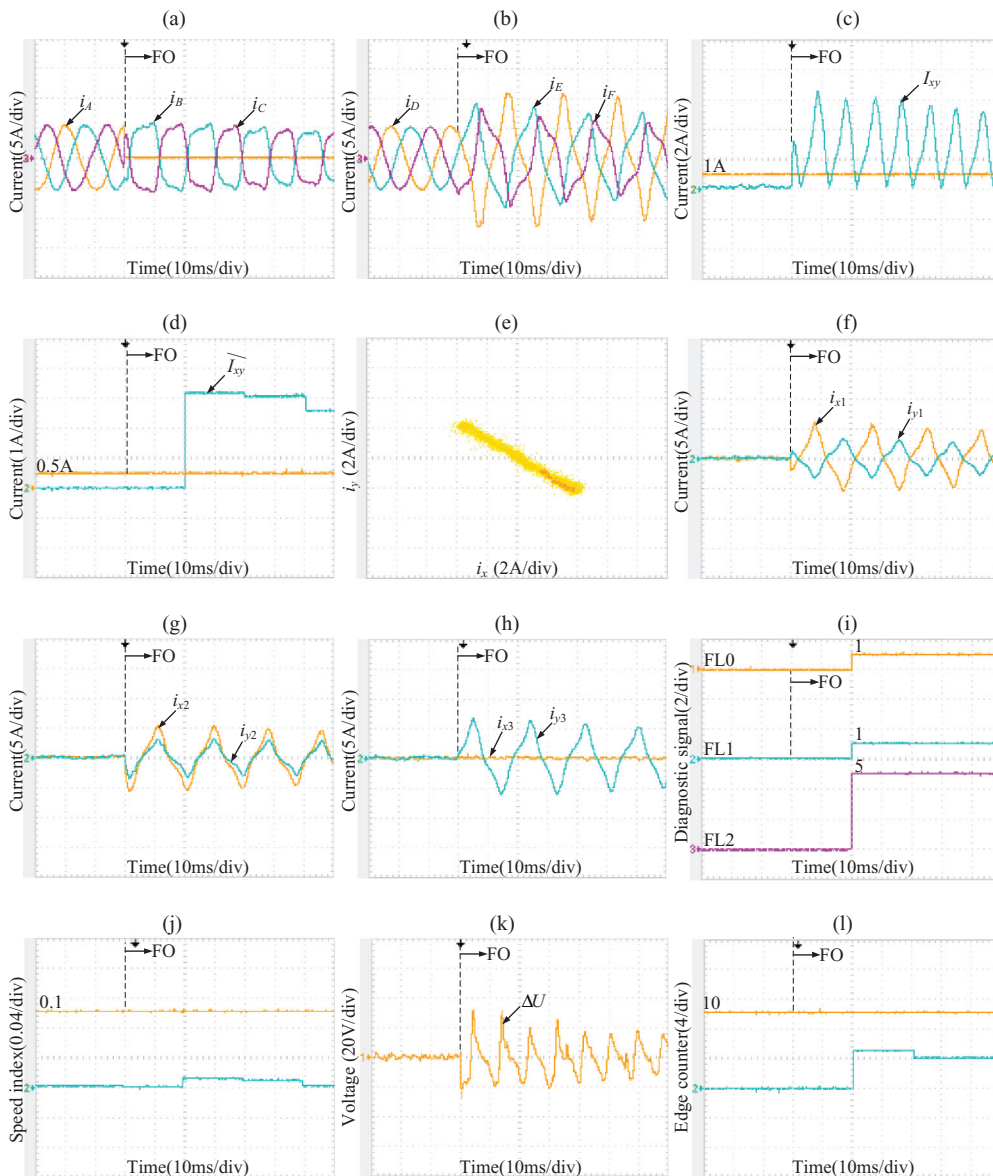


Fig. 11. Diagnostic process of current sensor fault in phase A: (a) phase currents of ABC; (b) phase currents of DEF; (c) amplitude of current on harmonic subspace; (d) current diagnosis; (e) current trajectory on harmonic subspace; (f) currents on $x1$ -axis and $y1$ -axis; (g) currents on $x1$ -axis and $y1$ -axis; (h) currents on $x1$ -axis and $y1$ -axis; (i) fault location signal; (j) speed diagnosis; (k) difference between voltage reference and estimated voltage; (l) voltage edge counter

7. Conclusion

A comprehensive investigation on the sensor fault diagnosis for T-type inverter-fed dual three-phase PMSM drives is conducted in this paper. A series of diagnostic methods have been proposed for the three types of sensor faults, including speed sensor fault, voltage sensor fault and current sensor fault. Both the sudden error change and gradual error change of sensor faults are considered. Firstly, the diagnosis of speed sensor fault was achieved by observing the error between the speed of stator flux and the value from speed sensor. Secondly, the large high-frequency voltage ripple of voltage difference between the estimated voltage and the reference voltage was used to identify the voltage sensor faults and the faulty voltage sensor was determined according to the deviation of voltage difference. Thirdly, the abnormal current amplitude on harmonic subspace was adopted to identify the current sensor faults and the faulty current sensor was located by distinguishing the current trajectory on x - y subspace under faulty state. The experimental results are given to verify the effectiveness of the proposed schemes.

References

- Bellini, A., Filippetti, F., Tassoni, C. and Capolino, G. A. (2008). Advances in Diagnostic Techniques for Induction Machines. *IEEE Transactions on Industrial Electronics*, 55(12), pp. 4109–4126.
- Berriri, H., Naouar, M. W. and Slama-Belkhdja, I. (2012). Easy and Fast Sensor Fault Detection and Isolation Algorithm for Electrical Drives. *Transactions on Power Electronics*, 27(2), pp. 490–499.
- Bojoi, R., Farina, F., Griva, G., Profumo, F. and Tenconi, A. (2005). Direct Torque Control for Dual Three-Phase Induction Motor Drives. *IEEE Transactions on Industry Applications*, 41(6), pp. 1627–1636.
- Choi, U. M., Blaabjerg, F. and Lee, K. B. (2015). Reliability Improvement of a T-type Three-Level Inverter with Fault Tolerant Control Strategy. *IEEE Transactions on Power Electronics*, 30(5), pp. 2660–2673.
- Choi, U. M., Lee, K. B. and Blaabjerg, F. (2014). Diagnosis and Tolerant Strategy of an Open-Switch Fault for T-Type Three-Level Inverter Systems. *IEEE Transactions on Industry Applications*, 50(1), pp. 495–508.
- Foo, G. H. B., Zhang, X. and Vilathgamuwa, D. M. (2013). A Sensor Fault Detection and Isolation Method in Interior Permanent-Magnet Synchronous Motor Drives Based on an Extended Kalman Filter. *IEEE Transactions on Industrial Electronics*, 60(8), pp. 3485–3495.
- Foo, G. H. B., Zhang, X. and Vilathgamuwa, D. M. (2015). Sensor Fault-Resilient Control of Interior Permanent-Magnet Synchronous Motor Drives. *IEEE Transactions on Mechatronics*, 20(2), pp. 855–864.
- Jahns, T. M. (1980). Improved Reliability in Solid-State AC Drives by Means of Multiple Independent Phase-Drive Units. *IEEE Transactions on Industry Applications*, 16(3), pp. 321–331.
- Levi, E., Barrero, F. and Duran, M. J. (2016). Multiphase Machines and Drives—Revisited. *IEEE Transactions on Industrial Electronics*, 63(1), pp. 429–432.
- Mengoni, M., Zarri, L., Tani, A., Parsa, L., Serra, G. and Casadei, D. (2015). High-Torque-Density Control of Multiphase Induction Motor Drives Operating Over A Wide Speed Range. *IEEE Transactions on Industrial Electronics*, 62(2), pp. 814–825.
- Najafabadi, T. A., Salmasi, F. R. and Jabejdar-Maralani, P. (2011). Detection and Isolation of Speed-, DC-Link Voltage-, and Current-Sensor Faults Based on an Adaptive Observer in Induction-Motor Drives. *IEEE Transactions on Industrial Electronics*, 58(5), pp. 1662–1672.
- Parsa, L. and Toliyat, H. A. (2007). Sensorless Direct Torque Control of Five-Phase Interior Permanent-Magnet Motor Drives. *IEEE Transactions on Industry Applications*, 43(3), pp. 952–959.
- Romary, R., Jelassi, S. and Brudny, J. F. (2010). Stator-Interlaminar-Fault Detection Using an External-Flux-Density Sensor. *IEEE Transactions on Industrial Electronics*, 57(1), pp. 237–243.
- Salmasi, F. R. (2017). A Self-Healing Induction Motor Drive with Model Free Sensor Tampering and Sensor Fault Detection, Isolation, and Compensation. *IEEE Transactions on Industrial Electronics*, 64(8), pp. 6105–6115.
- Sleszynski, W., Nieznanski, J. and Cichowski, A. (2009). Open-Transistor Fault Diagnostics in Voltage-Source Inverters by Analyzing the Load Currents. *IEEE Transactions on Industrial Electronics*, 56(11), 4681–4688.

- Umesh, B. and Sivakumar, K. (2016). Multilevel Inverter Scheme for Performance Improvement of Pole-Phase-Modulated Multiphase Induction Motor Drive. *IEEE Transactions on Industrial Electronics*, 63(4), pp. 2036–2043.
- Wang, X., Wang, Z, Cheng, M. and Hu, Y. (2017a). Remedial Strategies of T-NPC Three-Level Asymmetric Six-Phase PMSM Drives Based on SVM-DTC. *IEEE Transactions on Industrial Electronics*, 64(1), pp. 6841–6853.
- Wang, Z., Wang, Y., Chen, J. and Cheng, M. (2017b). Fault-Tolerant Control of NPC Three-Level Inverters-Fed Double-Stator-Winding PMSM Drives Based on Vector Space Decomposition. *IEEE Transactions on Industrial Electronics*, 64(11), pp. 8446–8458.
- Wang, Z., Wang, X, Cao, J., Cheng, M. and Hu, Y. (2018a). Direct Torque Control of T-NPC Inverters-Fed Double-Stator-Winding PMSM Drives With SVM. *IEEE Transactions on Power Electronics*, 33(2), pp. 1541–1553.
- Wang, Z., Wang, X, Cheng, M. and Hu, Y. (2018b). Comprehensive Investigation on Remedial Operation of Switch Faults for Dual Three-Phase PMSM Drives Fed by T-3L Inverters. *IEEE Transactions on Industrial Electronics*, 65(6), pp. 4574–4587.
- Zhao, Y. and Lipo, T.A. (1995). Space Vector PWM Control of Dual Three-Phase Induction Machine Using Vector Space Decomposition. *IEEE Transactions on Industry Applications*, 31(5), pp. 1100–1109.